



# Inverse design of multifunctional plasmonic metamaterial absorbers for infrared polarimetric imaging

JUNYU LI,<sup>1</sup> LI BAO,<sup>1</sup> SHUN JIANG,<sup>1</sup> QIUSHI GUO,<sup>2</sup> DEHUI XU,<sup>3</sup> BIN XIONG,<sup>3</sup>  
GUANGZU ZHANG,<sup>1</sup> AND FEI YI<sup>1,4,\*</sup>

<sup>1</sup>School of Optical and Electronic Information, Huazhong University of Science and Technology, Wuhan, 430074, China

<sup>2</sup>Department of Electrical Engineering, Yale University, New Haven, Connecticut 06511, USA

<sup>3</sup>Science and Technology on Micro-System Laboratory, State Key Laboratory of Transducer Technology, Shanghai Institute of Microsystem and Information Technology, Chinese Academy of Sciences, Shanghai 200050, China

<sup>4</sup>Shenzhen Huazhong University of Science and Technology Research Institute, Shenzhen, China

\*feiyi@hust.edu.cn

**Abstract:** Metamaterial absorbers, consisting of assembling arrays of optical resonators with subwavelength dimensions and spacing, allow efficiently absorption electromagnetic radiation by leveraging the strong electrical and magnetic resonances. Beyond the enhanced absorption, there is a growing interest to realize multi-functional absorbers, for example, absorbers with extended bandwidth, strong polarization extinction ratio, to name a few. Traditionally, designing multi-functional absorbers require complex brute-force optimizations with sizable parameter space, which turn out to be rather inefficient. Here, using the particle swarm optimization algorithm, we design and experimentally demonstrate broadband and highly polarization selective mid-IR metal-insulator-metal absorbers, covering the technologically important 3–5 μm atmospheric transparency band. With spectrally averaged absorption exceeding 70%, a high polarization extinction ratio of 40.6 is concurrently achieved by the algorithm. We also investigate the incident angle dependence of the spectral absorption and clarify the origin of optical losses. By integrating with the growing range of mid-IR detectors and imagers, our devices can enable new applications such as mid-IR full Stokes imaging polarimetry for remote sensing.

© 2019 Optical Society of America under the terms of the [OSA Open Access Publishing Agreement](#)

## 1. Introduction

Plasmonic metamaterial absorbers (PMAs) are capable of trapping light, enhancing the near-field via the localized surface plasmon resonances (LSPR) excited in the constituent metallic subwavelength resonators and in turn, efficiently converting the incident electromagnetic radiations into heat [1–4]. PMAs can thus adapt to a wide range of applications across the electromagnetic spectrum, such as thermal detectors and emitters [5–7], optical sensing [8,9], thermal photovoltaic [10–14], encoding and display [15,16] and photothermal medical therapy [17–21]. Compared to conventional photonic structures such as Fabry-Perot or photonic crystal cavities, PMA offers more degrees of freedom in terms of controlling the light-matter interaction, making it a versatile platform to realize a suite of new functionalities in addition to enhancing the absorption. For instance, by engineering the geometric sizes and patterns of the subwavelength resonators, one can mold the waveform and polarization state of light after interacting with the subwavelength resonators [22–24]. With judicious design, it is also possible to realize high absorption concurrently with broadband operation [25,26], which is sought-after for applications such as room-temperature mid-IR detection and sensing.

The traditional way of designing PMAs for a specific application is to select an overall structure based on existing physical principles and intuition, and then iteratively fine-tune the structure by brute-force parameter sweep simulations [26–29]. For PMAs with a simple structure and functionality, the hand-tuning method may cover the full design space. However, in order to realize multifunctional PMAs, the structure of PMAs have to become increasingly complicated. The increasing number of parameters makes it very challenging for the designer to manually explore the full design space and to obtain the optimal design. To handle the design problems of nanophotonic devices with ever increasingly complicated structures, several computational inverse design algorithms have been developed to allow automated design and optimization of nanophotonic devices with user-defined performance specifications. Successful examples include bandgap optimization in photonic crystals [30,31], mode coupling optimization in waveguide geometries [32–34], nonlinear optics in engineered nanostructures [35,36], metasurface based flat optics [37,38].

In this work, we implement the particle swarm optimization algorithm (PSO) [39,40], a robust and easy-to-implement computational algorithm to demonstrate the design of PMAs with a broad spectral range (from  $3\mu\text{m}$ – $5\mu\text{m}$ ) of high absorption and high polarization extinction ratios. Importantly, such PMAs not only combine the functionalities of conventional optical filters and polarizers, but also can be implanted into optoelectronic devices as an integral part. For example, by integrating the multifunctional PMAs onto the pixels of the commercially available uncooled focal plane array (FPA) such as microbolometers, the FPAs can resolve the wavelengths and polarization states of the electromagnetic radiation at the pixel level, thus mitigating the need for conventional optical filters and polarizers. Eventually, novel applications such as snapshot polarimetric imaging and hyperspectral imaging in the mid-infrared frequencies can be realized by individually tailoring the optical response of each pixel across the FPA using the integrated PMA [41–45].

## 2. Results and discussion

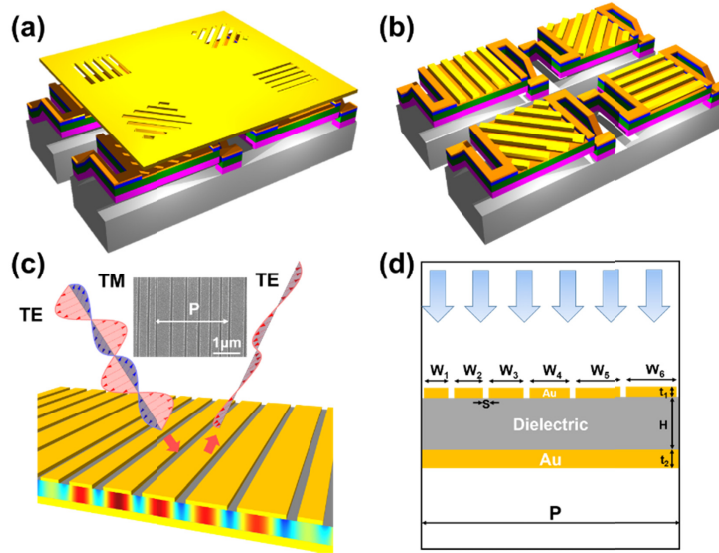


Fig. 1. (a) Micro-polarizer based polarization imaging architecture. (b) PMAs based polarization imaging architecture (c) and (d) Schematic diagram of the proposed three-layered optimized absorber. The inset of (c) shows the SEM image of the fabricated sample with  $P = 2.672 \mu\text{m}$ ,  $t_1 = 50 \text{ nm}$ ,  $t_2 = 100 \text{ nm}$ , and  $H = 67.5 \text{ nm}$ . Strip widths (from  $W_1$  to  $W_6$ ) form an arithmetic sequence, with average width  $W = 386.7 \text{ nm}$ , the difference  $\Delta = 54.3 \text{ nm}$ , and the spaces  $S = 58.7 \text{ nm}$ .

The concept of polarization selective PMA with broad spectral absorption band and its application in polarimetric imaging are illustrated in Fig. 1. As shown by Fig. 1(a), the traditional way of resolving the polarization state with intensity measurement is to put a  $2 \times 2$  array of micro-polarizers in front of a super-pixel which consists of four pixels [45,46]. Following the Stokes formalism, the transmission axis of each micro-polarizer is placed at  $0^\circ$ ,  $45^\circ$ ,  $90^\circ$  and  $135^\circ$ , while the corresponding readouts of the four pixels are  $I_0$ ,  $I_{45}$ ,  $I_{90}$  and  $I_{135}$ , respectively [41]. The Stokes parameters are then calculated as:

$$S_0 = \frac{I_0 + I_{45} + I_{90} + I_{135}}{2}, \quad (1)$$

$$S_1 = I_0 - I_{90}, \quad (2)$$

$$S_2 = I_{45} - I_{135}, \quad (3)$$

Here  $S_0$  indicates the total light intensity arriving at the super-pixel.  $S_1$  gives the amount of horizontal or vertical linear polarization and  $S_2$  gives the amount of linear polarization in the  $45^\circ$  or  $135^\circ$  direction. The polarization state of incident light can then be described using the degree of linear polarization (DoLP) and the angle of polarization (AoP):

$$DoLP = \frac{\sqrt{S_1^2 + S_2^2}}{S_0}, \quad (4)$$

$$AoP = \frac{1}{2} \tan^{-1} \frac{S_2}{S_1}, \quad (5)$$

To generate nice images of a target, a focal plane array with high pixel counts, e.g.  $512 \times 512$  pixels, is usually needed [45]. Due to the ability to image not only the intensity but also the polarization states of electromagnetic radiation from the target, polarimetric imaging extends the capabilities of conventional imaging techniques based on intensity measurement and enables new imaging modalities that find a wide range of applications in remote sensing, atmospheric detection, earth sources investigation, medical diagnostic, military target detection and identification, imaging comprehension, and computer vision [43,47]. The micro-polarizer array based polarization imager has been demonstrated in the infrared range ( $3\mu\text{m}$ – $5\mu\text{m}$ ) in the 1990s [45,48] and then extended to the visible region [41,42,49]. However, due to the inevitable air gap between the micro-polarizer and the pixel, the micro-polarizer array-based architecture suffers from cross-talk and reduced polarization extinction ratio when the light is incident at an angle, as illustrated by Fig. 2(c) [47,50]. An effective method to circumvent this effect is to have PMAs directly integrated with the pixels of infrared detectors to tailor their spectral selectivity and polarization extinction ratio. Importantly, due to the excitation of localized magnetic resonances [51,52], the spectral absorption of PMAs are insensitive to the incident angle of light. Figure 1(b) shows the conceptual drawing of four microbolometers integrated with PMAs for resolving the polarization state of infrared radiation. Since the PMAs are directly fabricated on to the pixels, there exists no air gap between the PMA and the pixel. The PMA consists of a top layer of metallic nanostrip antennas atop a dielectric spacer and a metallic backplate, as shown in Fig. 1(c). The nanostrip antenna based metal-insulator-metal (MIM) structure can selectively absorb the TM polarization while reflecting the TE polarization of the incident radiation. Due to the free carrier absorption in the nanostructured metals, the absorbed optical energy is eventually converted into heat which then elevates the temperature of the microbolometers beneath [53,54]. The simplest version of the nanostrip antenna based MIM absorber has a top layer of single-sized nanostrips arranged in a periodic pattern. By hand-tuning the width of the nanostrip and the period of the pattern, polarization selective near-unity absorption has been demonstrated across the infrared range [8,10,26,29,52,55–57]. However, the spectral

absorption of the single-sized nanostrip antenna absorber is generally narrow, unable to cover the two atmospheric windows in the mid-infrared range: 3  $\mu\text{m}$ –5  $\mu\text{m}$  and 8  $\mu\text{m}$ –14  $\mu\text{m}$ . To broaden the spectral absorption band, multi-sized antenna absorber with four different nanostrip widths has been explored and high absorption from 8.5  $\mu\text{m}$  to 11.5  $\mu\text{m}$  was demonstrated [26]. However, only the tuning difference  $\Delta$  between the nanostrip widths was varied by hand to tune the spectral absorption while other parameters were kept unchanged. Also the achieved polarization extinction ratio is less than 20 [26].

To further improve the absorber performances including the bandwidth and the polarization extinction ratio, we dig deeper into the parameter space by using the PSO algorithm to vary and optimize four parameters of the multi-sized nanostrip antenna absorber: the spacing ( $S$ ) between adjacent strips, the tuning difference ( $\Delta$ ), the thickness of dielectric spacer ( $H$ ) and the average width of the nanostrip ( $W$ ), as shown in Fig. 1(d). The four optimization parameters form a vector  $X = [S, \Delta, H, W]$ , which is called the *particle* structure. The values of the four parameters are the *coordinates* which determine the *position* of the particle in the 4-dimensional *solution space*. To search through the solution space, we designate 20 particles and the entire collection of the 20 particles is called a *swarm*. The goodness of the position of each particle is evaluated by a *fitness function* (FF). Since we aim at a highly polarization extinction ratio and a high absorption in the 3  $\mu\text{m}$ –5  $\mu\text{m}$  band, the fitness function has the following expression:

$$\text{FF} = \frac{\int_{\lambda=3\mu\text{m}}^{\lambda=5\mu\text{m}} A_{\text{TM}}(\lambda) d\lambda}{\int_{\lambda=3\mu\text{m}}^{\lambda=5\mu\text{m}} A_{\text{TE}}(\lambda) d\lambda}. \quad (6)$$

Here  $A_{\text{TM}}(\lambda)$  and  $A_{\text{TE}}(\lambda)$  are the spectral absorption of TM polarization and TE polarization, respectively and the value of the FF (fitness value) is obtained by dividing the integration of  $A_{\text{TM}}(\lambda)$  by the integration of  $A_{\text{TE}}(\lambda)$  in the 3  $\mu\text{m}$ –5  $\mu\text{m}$  band. The algorithm initiates by assigning each particle with a random location and a random velocity. Then the swarm iteratively searches the solution space for the optimal position by tracking two “best values”. One is the optimal solution found by the particle itself, called the personal best  $p_i$ , and the other is the optimal solution found by the entire group, called global best  $p_g$ . Assuming the population size of the swarm is  $M$  and the dimension of the search space is  $D$ , the  $i_{\text{th}}$  particle ( $i = 1, 2, \dots, M$ ) in the swarm will update its position  $x_i$  and velocity  $v_i$  according to the following formula:

$$v_{iD}^{k+1} = w v_{iD}^k + c_1 \xi(p_{iD}^k - x_{iD}^k) + c_2 \eta(p_{gD}^k - x_{iD}^k), \quad (7)$$

$$x_{iD}^{k+1} = x_{iD}^k + v_{iD}^{k+1} \Delta t. \quad (8)$$

As suggested by [58], in the velocity updating, a time-varying inertia weight  $w$  decreases linearly from 0.9 to 0.4 through iterations (the max iteration is 50). In this work, the number of particles  $M$  in the swarm is fixed to be 20. Each component in matrices  $\xi$  and  $\eta$  has a uniform distribution in (0, 1) to ensure the randomness. Constants  $c_1$  and  $c_2$  both take a value of 1.49 to balance the cognitive and social influences [40].

The electromagnetic fields in the multi-sized nanostrip antenna absorber and the corresponding spectral absorption are obtained using Lumerical, a finite difference time domain (FDTD) method based solver. As shown in Fig. 1(d), due to the periodicity of the physical structure, only one period of the whole structure is simulated with periodic boundary conditions applied at the left and right side of the unit cell. A normally incident plane wave source is applied above the structure as the excitation and a power monitor is used to collect the reflected waves and calculate the power reflection coefficient  $R$ . Since the gold backplate of MIM structure is made thick enough to eliminate the transmission ( $T = 0$ ), the calculation of the power absorption coefficient  $A$  is simplified to  $A = 1 - R$ . The dispersive complex

dielectric constants of gold (Au) is obtained from [59]. The simulation time is 10000 fs and the convergence criteria were set to be with auto shutoff min of  $10^{-6}$ . The cross-section of the electric field and magnetic field distribution was detected by a 2D field profile monitors in x-z plane. Both the TE polarization and TM polarization are simulated to obtain  $A_{\text{TM}}(\lambda)$  and  $A_{\text{TE}}(\lambda)$  and the fitness value is then calculated using Eq. (6). In each round of search, the fitness values calculated in FDTD solutions are passed to the home made PSO codes written in MATLAB script to update the positions and velocities of the particles. The updated particles are then passed back to FDTD solutions and the geometric parameters  $[S, \Delta, H, W]$  are adjusted accordingly for a new iteration.

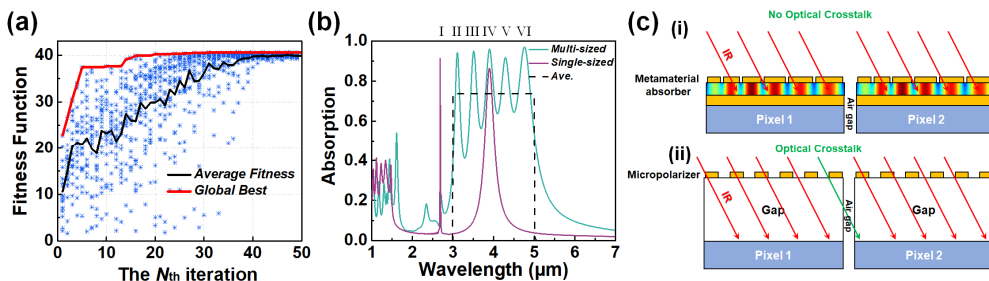


Fig. 2. (a) Evolution of the fitness values as a function of the number of iterations during the PSO optimization by using 20 particles for 50 iterations. Blue star markers represent the fitness values of the 20 particles in each iteration. The “average fitness” represents the averaged fitness value of the 20 particles in each iteration and the “global best” records the largest value of the “current best” since the first iteration. (b) Comparison of the absorption spectra between the absorber with multi-sized nanostrips and the single-sized nanostrip absorber. Mark I to VI stand for six absorption peaks of the absorber with multi-sized nanostrips, respectively. (c) Comparison between (i) the PMA based architecture and (ii) the micro-polarizer based architecture and regarding the optical crosstalk. For the PMA based architecture, the metamaterial absorber converts the incident electromagnetic waves into heat directly to the corresponding pixels, and there is no significant optical crosstalk between adjacent pixels under oblique incidence. For the micro-polarizer based architecture, due to the air gap between the micropolarizer and the pixel, the obliquely incident wave could penetrate the micropolarizer above a pixel (Pixel 1) and hit its neighboring pixel (Pixel 2), thus leading to crosstalk [47,50].

Figure 2 illustrates an example of PSO search for a broadband polarization selective MIM absorber with multi-sized nanostrip antenna structure. Here we implement 6 nanostrips into a unit cell of the periodic structure and use amorphous silicon as the spacing material. The number N of particles is 20 and the number of iterations is 50. Both TM polarization and TE polarization are calculated and the total number of FDTD simulation is therefore  $20 \times 50 \times 2 = 2000$ . As shown by Fig. 2(a), the initial global best fitness value  $p_g$  is less than 25. After 50 rounds of iterations,  $p_g$  finally grows to 40. Also, the fitness values of the 20 particles converge to  $p_g$  after 50 rounds of iterations. The computationally optimized spectral absorption of the TM polarization is shown by the green solid line in Fig. 2(b). We labeled the wavelengths of six resonant peaks caused by the LSPR using I, II, III, IV, V and VI. It is observed that the excited surface plasmon polariton (SPP) at 2.7 μm deteriorates the resonant peak I. The averaged TM absorption in the 3 μm–5 μm range is 73.7% and the fitness value is 40.58. As a comparison, we also plot the spectral absorption of the MIM absorber with a single sized antenna using the purple solid line. Similarly, the absorption peak at around 3.9 μm is caused by the LSPR and the very sharp absorption peak at around 2.7 μm is due to the excited SPP. The averaged TM absorption of the single sized antenna absorber in 3 μm–5 μm range is only 18.5% and the fitness value is 9.3. In other words, the averaged absorption of the optimized multi-sized antenna absorber is 4 times larger than the single sized antenna absorber. It is worth noting that the period of the optimized multi-sized antenna absorber is 2.672 μm, which is nearly 7 times the average nanostrip width of 386.7 nm. This indicates

that the structure has a large absorption cross-section, which is one of the reasons why this structure can achieve broadband absorption [26].

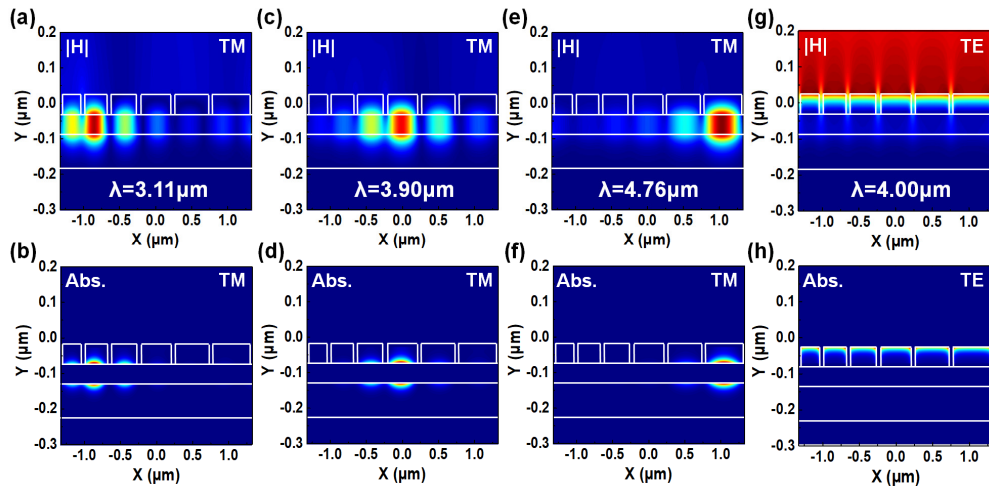


Fig. 3. The distribution of the normalized magnetic field magnitude  $|H|$  in the optimized structure under TM polarization at (a) peak II (c) peak IV and (e) peak VI of the spectral absorption shown in Fig. 2(b). Fig. (b), (d) and (f) show the corresponding normalized absorption intensity distribution. (g) The distribution of  $|H|$  under TE polarization at  $\lambda = 4\mu\text{m}$  and (h) the corresponding distribution of absorption intensity.

To further reveal the mechanism of broadband absorption and polarization extinction ratio of the computer optimized structure, we plot in Figs. 3(a)-3(f) the local distribution of magnetic field intensity and the corresponding optical energy loss of the TM polarization at three resonant wavelengths:  $3.11\mu\text{m}$ ,  $3.90\mu\text{m}$  and  $4.76\mu\text{m}$ , respectively. It is clearly shown that at each resonance, the local magnetic fields are mainly confined in the spacer under one nanostrip and the local fields under other nanostrips are weak. As the resonant wavelength increases from  $3.11\mu\text{m}$  to  $4.76\mu\text{m}$ , the concentrated local magnetic fields move from the 2nd nanostrip to the 6th nanostrip. Correspondingly, the optical energy loss is mainly concentrated in one nanostrip and the backplate below that nanostrip at each resonance. Therefore, the broadband absorption of the TM polarization in the  $3\mu\text{m}-5\mu\text{m}$  range is mainly caused by the LSPRs excited from the second nanostrip to the fifth nanostrip of the optimized structure. The lowered absorption peak at  $2.67\mu\text{m}$  results from the excited SPP which deteriorates the LSPR mode under the first nanostrip [60]. To understand the optical absorption in the TE polarization, we then plot the local magnetic field intensity and optical energy loss of TE polarization at  $4\mu\text{m}$  in Fig. 5(g) and 5(h), respectively. It is found that TE-polarized electromagnetic fields can penetrate into the metallic nanostrips and this causes optical energy loss at the top surface of the nanostrips. Consequently, there exists a small amount ( $\sim 2\%$ ) of optical absorption in the TE polarization. We note that the optical absorption in the TE polarization is an important limiting factor of the polarization extinction ratio because even if the averaged absorption in the TM polarization is 100%, a 2% of absorption in TE polarization will lead to a fitness value of only 50. Therefore, to further improve the polarization extinction ratio, the absorption in TE polarization needs to be minimized. Potential ways of minimizing the absorption of TE polarization include increasing the thickness of the nanostrips and replacing gold with aluminum or silver.

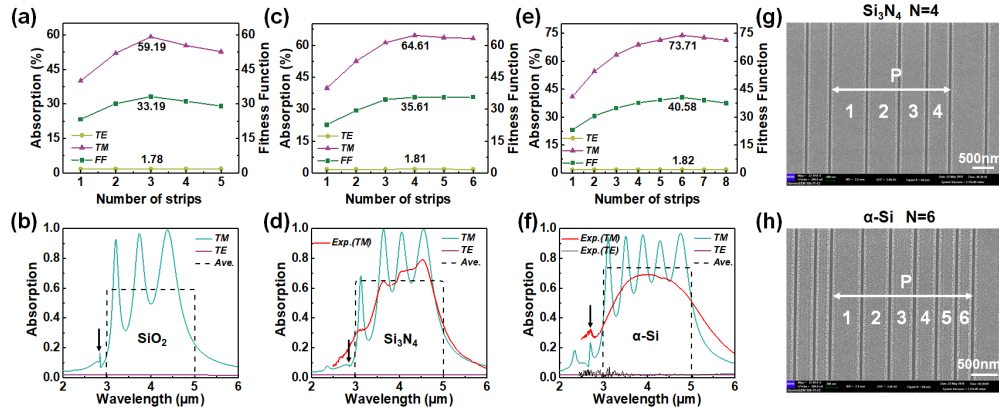


Fig. 4. The spectral absorption of the TE polarization (yellow line) and TM polarization (purple line) and the corresponding FF (green line) as a function of the number of nanostrips per period assuming (a) silicon dioxide (c) silicon nitride and (e) amorphous silicon ( $\alpha\text{-Si}$ ) as the spacing material. The optimal number of nanostrips per period and the corresponding maximal FFs are also labeled in the plots. (b), (d) and (f) show the absorption spectra of TE polarization and TM polarization corresponding to (a), (c) and (e), assuming the number of nanostrips per period is 3, 4 and 6, respectively. The black arrows point out the influence of the excited SPP. The black dash lines show the averaged absorption of the TM polarization in the 3  $\mu\text{m}$ –5  $\mu\text{m}$  range. (g) and (h) SEM images of the optimized absorbers with silicon nitride and amorphous silicon as the spacing materials.

We then examine the influence of the number of nanostrips per period and the spacing material on the optimized spectral absorption, by choosing silicon dioxide, silicon nitride and amorphous silicon ( $\alpha\text{-Si}$ ) as the spacing materials. The refractive index of silicon dioxide is taken from [59], while the refractive index of silicon nitride and  $\alpha\text{-Si}$  are obtained by ellipsometry measurement (See Fig. 6 in the Appendix for the measured refractive indices of silicon nitride and  $\alpha\text{-Si}$ ). The trends of the spectrally averaged absorption and the fitness values as a function of the number of nanostrips per period plotted in Figs. 4(a)-4(c) show that there exists an optimal number of nanostrips and a corresponding maximal fitness value for each spacing material. For example, for silicon dioxide spacer, using three nanostrips with different widths in one period can achieve the highest average TM polarization absorption of 59.19% and the maximal fitness value of 33.19. Correspondingly, there exist 3 peaks in the optimized TM absorption spectrum in the 3–5  $\mu\text{m}$  range, as shown by Fig. 4(b). For silicon nitride, the optimal number of nanostrips per period is 4 while the resulted average TM polarization absorption is 64.61% and the maximal fitness value is 35.61. The corresponding optimized spectral absorption plotted in Fig. 4(d) has 4 peaks in the 3  $\mu\text{m}$ –5  $\mu\text{m}$  range. When amorphous silicon is used as the spacing material, the highest average TM polarization absorption of 73.71% and fitness value of 40.58 can be achieved with six nanostrips per period. However, due to the excitation of SPP, only 5 peaks appear in the TM absorption spectrum in the 3  $\mu\text{m}$ –5  $\mu\text{m}$  range.

To experimentally verify the numerical results, we fabricated the inversely designed MIM absorbers, using silicon nitride and amorphous silicon as the spacing materials, respectively. The fabrication begins with E-beam deposition of a 100 nm thick layer of gold on a single-sided polished silicon substrate. Thereafter, a layer of dielectric spacer was deposited on the gold layer by plasma enhanced chemical vapor deposition (PECVD). Another adhesion layer of 5 nm titanium and 50 nm thick layer of gold was E-beam evaporated followed by PECVD. A layer of e-beam resist (AR-P 6200.09) was then spin coated on top and patterned using E-beam lithography. After exposure, the sample was developed in developer AR 600-60 for 70 s and stopper AR 600-546 for 35 s to generate the patterns. Then, the patterns were transferred to the top gold layer by RIE etching. Finally, a standard oxygen plasma etching process was used to remove the residual resist. The SEM images of the fabricated nanostrip antennas on

top of the MIM absorbers are shown in Fig. 4(g) and Fig. 4(h). The reflectance spectra of the fabricated MIM absorbers were characterized from a wavelength of 2–16  $\mu\text{m}$  using a Fourier transform infrared (FTIR) spectrometer (VERTEX 70 from Bruker) combined with an IR microscope (Hyperion 2000). The area of each nanoantenna array on top of the absorber is 500  $\mu\text{m} \times 500 \mu\text{m}$ , and the aperture size of the FTIR is 300  $\mu\text{m} \times 300 \mu\text{m}$ . The infrared beam is polarized by a MIR wire grid polarizers (Thorlabs, WP25M-IRC), with transmittance above 50% from 2.5  $\mu\text{m}$  to 16  $\mu\text{m}$ . The measured reflection spectra are normalized with respect to a gold mirror (Thorlabs, PF05-03-M01) while the transmission spectrum is considered to be zero. The measured reflectance are then used to calculate the absorbance. The measured absorption spectra of the optimized absorbers with silicon nitride and  $\alpha$ -Si as the spacing materials are also plotted in Fig. 4(d) and Fig. 4(f). The measured absorption spectra of the TM mode and TE mode confirm that the fabricated MIM absorber can achieve a large polarization extinction ratio in a broad spectral range, as predicted by the numerical simulation. However, the measured absorption spectra do not accurately reproduce the fine features in the simulated absorption spectra such as the individual absorption peaks in the TM modes. This is attributed to the fact that the roughness at the edges of the fabricated nanostrips.

**Table 1.** Relevant parameters of the optimized absorbers with three spacing materials

Material	N	S (nm)	Delta (nm)	H (nm)	W (nm)	FF	A <sub>TM</sub> (%)	A <sub>TE</sub> (%)	P ( $\mu\text{m}$ )	P/W	Ratio
SiO <sub>2</sub>	3	77.6	184.8	59.7	871.1	33.19	59.19	1.78	2.846	3.267	0.918
Si <sub>3</sub> N <sub>4</sub>	4	69.5	104.5	68.5	646.6	35.61	64.61	1.81	2.864	4.430	0.903
$\alpha$ -Si	6	58.7	54.3	67.5	386.7	40.58	73.71	1.82	2.672	6.912	0.868

Table 1 summarizes the relevant parameters of the optimized absorbers with the three spacing materials. Here  $W$  is the average width of the  $N$  nanostrip in a period of the structure and  $\text{Ratio} \equiv N \cdot W/P$  is the ratio of the total width of the  $N$  nanostrips to the period  $P$ . It is seen that by increasing the refractive index of the spacer, the average nanostrip width  $W$  is reduced and therefore more nanostrips can be packed into a period of the structure to improve the absorption  $A_{\text{TM}}$  of the TM polarized waves. However, there is always a small amount of absorption  $A_{\text{TE}}$  of the unwanted TE-polarized waves from 3  $\mu\text{m}$  to 5  $\mu\text{m}$ , which is due to the finite conductivity of gold in this frequency range. The results also show that with the increase of  $\text{Ratio}$ ,  $A_{\text{TE}}$  will decrease and eventually approach the absorption rate of a continuous top layer of gold. The small amount of TE absorption  $A_{\text{TE}}$  is therefore an important limiting factor of the fitness value  $FF$ . We also notice that the periods of the optimized absorbers with the three spacing materials are all less than 3  $\mu\text{m}$ . This is because when the period  $P$  is close to the working wavelength (3  $\mu\text{m}$ –5  $\mu\text{m}$ ), the excited SPP will deteriorate the LSPR [60] and significantly lower the spectral absorption and the “particles” try to avoid the structures with  $P > 3 \mu\text{m}$  during the PSO search.

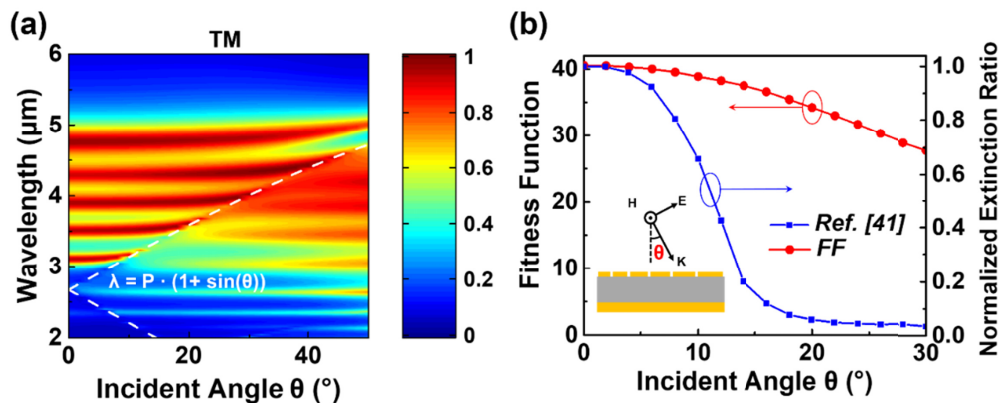


Fig. 5. (a) The spectral absorption of the optimized absorber as a function of the incident angle. The white dash line stands for the resonant wavelength of the surface plasmon polariton excited in the structure as a function of the incident angle. (b) The red solid line stands for the FF as a function of incident angle of the impinging light as compared to the blue solid line showing the incident angle dependence of the normalized polarization extinction ratio of the micro-polarizer [41].

To effectively tailor the spectral selectivity and polarization extinction ratio of the microbolometer towards polarization imaging, the integrated PMA should maintain a broadband high absorption and large polarization extinction ratio within a wide range of incident angle. We then analyze the spectral absorption of the optimized absorber as a function of the incident angle of the plane wave excitation. A broadband plane wave source of the FDTD solver is used to excite the unit cell of the periodic structure at oblique incidence angle and a power monitor is used to collect the reflected waves. The spectral absorption of the TM polarized waves shown in Fig. 5(a) can maintain a high value in a wide angular range due to the excited LSPR. We also observed that as the incident angle increases, the excited SPPs will perturb the absorption from the LSPR, as indicated by the white dash line in Fig. 5(a). We then look into the incident angle dependence of the polarization extinction ratio. As shown by the red solid line in Fig. 5(b), when the incident angle increases from 0° to 30°, the fitness value decreases from 40 to 28. In other words, the fitness value at 30° incidence is still 70% of the fitness value at 0° incidence. As a comparison, the blue line plots the normalized polarization extinction ratio of the micro-polarizer based architecture as a function of the incident angle taken from [41]. It is seen that the polarization extinction ratio rapidly decreases when the incident angle is above 5° and approaches zero when the incident angle is greater than ~20°. This clearly shows that the polarization selective PMA based architecture can effectively improve the incident-angle tolerance of the polarization extinction ratio compared to the micro-polarizer based architecture.

### 3. Conclusion

In summary, PMAs are a compact and versatile platform for directly tailoring the optical responses of infrared FPAs at the pixel level without the need of multiple optical components such as optical filters and polarizers, thus holding promise for revolutionizing the infrared imaging systems that are currently complex, bulky and expensive. In particular, we use the home made PSO codes to inversely design a PMA that can simultaneously achieve spectral selectivity and polarization extinction ratio with a wide incident angle tolerance. The absorber based on the MIM structure with multi-sized nanostrip antennas as the top layer is computationally optimized by varying the spaces between adjacent strips, the tuning difference, the thickness of dielectric spacer and the average width of the nanostrip. We also systematically investigated the spectral absorption and the polarization extinction ratio as a function of the number of nanostrips  $N$  in a period, the refractive index of the spacing

materials and the incident angle. The optimized absorber can achieve an average absorption above 70% from 3  $\mu\text{m}$ –5  $\mu\text{m}$  with a polarization extinction ratio of 40.6 under normal incidence. When the incident angle is 30° the average absorption from 3  $\mu\text{m}$ –5  $\mu\text{m}$  and the corresponding polarization extinction ratio can still maintain at 70% and 28, respectively. We emphasize that the spectral range of high absorption can also be inversely designed to cover other important IR bands such as the atmospheric window of 8  $\mu\text{m}$ –14  $\mu\text{m}$ . Therefore, when integrated with the pixels of microbolometer based IR FPAs, the multifunctional PMAs can replace the bandpass filters and micro-polarizers and enable compact multi-band IR polarimetric imagers.

#### Appendix A: The refractive indices of silicon dioxide, silicon nitride and $\alpha$ -Si

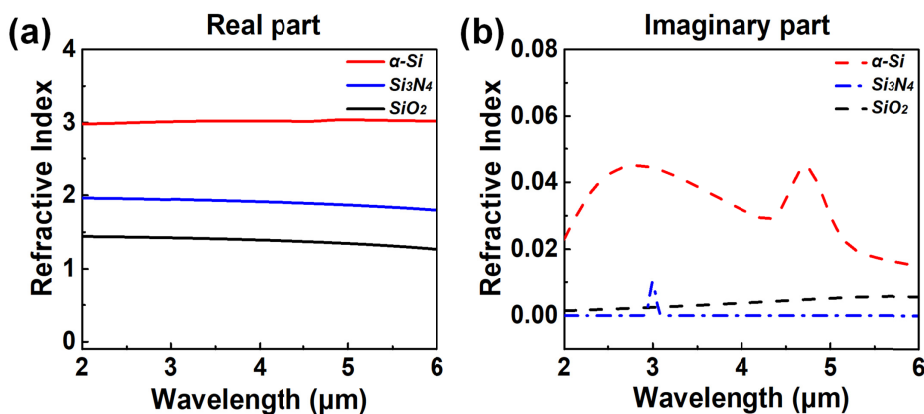


Fig. 6. The refractive index of silicon dioxide is from reference [59], while the refractive index of silicon nitride and  $\alpha$ -Si are obtained by ellipsometry measurement (IR-VASE II from J.A. Woollam).

#### Funding

National Natural Science Foundation of China (NSFC) (11604110, 11774112); National key research and development program of China (2016YFC0201300); Fund from Science, Technology and Innovation Commission of Shenzhen Municipality (JCYJ20160429182829578); The Fundamental Research Initiative Funds for Huazhong University of Science and Technology (2017KFYXJJ031, 2018KFYYXJJ052).

#### Acknowledgments

We thank Li Pan engineer in the Center of Micro-Fabrication and Characterization (CMFC) of WNLO for the support in PECVD fabrication. We thank Zeng Tiantian engineer in the Huazhong University of Science & Technology Analytical & Testing Center for the support in FTIR test. We thank the technical support from Experiment Center for Advanced Manufacturing and Technology in School of Mechanical Science & Engineering of HUST.

#### References

1. C. M. Watts, X. Liu, and W. J. Padilla, "Metamaterial electromagnetic wave absorbers," *Adv. Mater.* **24**(23), OP98–OP120, OP181 (2012).
2. L. Novotny and N. Van Hulst, "Antennas for light," *Nat. Photonics* **5**(2), 83–90 (2011).
3. K. B. Crozier, A. Sundaramurthy, G. S. Kino, and C. F. Quate, "Optical antennas: Resonators for local field enhancement," *J. Appl. Phys.* **94**(12), 7950 (2003).
4. Y. Cui, Y. He, Y. Jin, F. Ding, L. Yang, Y. Ye, S. Zhong, Y. Lin, and S. He, "Plasmonic and metamaterial structures as electromagnetic absorbers," *Laser Photonics Rev.* **8**(4), 495–520 (2014).
5. F. Yi, H. Zhu, J. C. Reed, and E. Cubukcu, "Plasmonically enhanced thermomechanical detection of infrared radiation," *Nano Lett.* **13**(4), 1638–1643 (2013).

6. F. Yi, H. Zhu, J. C. Reed, A. Y. Zhu, and E. Cubukcu, "Thermoplasmonic Membrane-Based Infrared Detector," *IEEE Photonics Technol. Lett.* **26**(2), 202–205 (2014).
7. J. Y. Suen, K. Fan, J. Montoya, C. Bingham, V. Stenger, S. Sriram, and W. J. Padilla, "Multifunctional metamaterial pyroelectric infrared detectors," *Optica* **4**(2), 276–279 (2017).
8. N. Liu, M. Mesch, T. Weiss, M. Hentschel, and H. Giessen, "Infrared perfect absorber and its application as plasmonic sensor," *Nano Lett.* **10**(7), 2342–2348 (2010).
9. A. Y. Zhu, F. Yi, J. C. Reed, H. Zhu, and E. Cubukcu, "Optoelectromechanical multimodal biosensor with graphene active region," *Nano Lett.* **14**(10), 5641–5649 (2014).
10. C. Wu, B. Neuner III, J. John, A. Milder, B. Zollars, S. Savoy, and G. Shvets, "Metamaterial-based integrated plasmonic absorber/emitter for solar thermo-photovoltaic systems," *J. Opt.* **14**(2), 024005 (2012).
11. E. Rephaeli and S. Fan, "Absorber and emitter for solar thermo-photovoltaic systems to achieve efficiency exceeding the Shockley-Queisser limit," *Opt. Express* **17**(17), 15145–15159 (2009).
12. D. N. Woolf, E. A. Kadlec, D. Bethke, A. D. Grine, J. J. Nogan, J. G. Cederberg, D. Bruce Burkel, T. S. Luk, E. A. Shaner, and J. M. Hensley, "High-efficiency thermophotovoltaic energy conversion enabled by a metamaterial selective emitter," *Optica* **5**(2), 213–218 (2018).
13. A. Lenert, D. M. Bierman, Y. Nam, W. R. Chan, I. Celanović, M. Soljačić, and E. N. Wang, "A nanophotonic solar thermophotovoltaic device," *Nat. Nanotechnol.* **9**(2), 126–130 (2014).
14. P. Bermel, M. Ghebrebrhan, W. Chan, Y. X. Yeng, M. Araghchini, R. Hamam, C. H. Marton, K. F. Jensen, M. Soljačić, J. D. Joannopoulos, S. G. Johnson, and I. Celanovic, "Design and global optimization of high-efficiency thermophotovoltaic systems," *Opt. Express* **18**(19 Suppl 3), A314–A334 (2010).
15. Z.-H. Wang, Y.-S. Hu, X. Xiong, R.-W. Peng, and M. Wang, "Encoding and display with stereo split-ring resonator arrays," *Opt. Lett.* **42**(6), 1153–1156 (2017).
16. A. Chanana, A. Paulsen, S. Guruswamy, and A. Nahata, "Hiding multi-level multi-color images in terahertz metasurfaces," *Optica* **3**(12), 1466–1470 (2016).
17. P. Fortina, L. J. Kricka, D. J. Graves, J. Park, T. Hyslop, F. Tam, N. Halas, S. Surrey, and S. A. Waldman, "Applications of nanoparticles to diagnostics and therapeutics in colorectal cancer," *Trends Biotechnol.* **25**(4), 145–152 (2007).
18. A. M. Gobin, M. H. Lee, N. J. Halas, W. D. James, R. A. Drezek, and J. L. West, "Near-infrared resonant nanoshells for combined optical imaging and photothermal cancer therapy," *Nano Lett.* **7**(7), 1929–1934 (2007).
19. H. Kim, S. Beack, S. Han, M. Shin, T. Lee, Y. Park, K. S. Kim, A. K. Yetisen, S. H. Yun, W. Kwon, and S. K. Hahn, "Multifunctional Photonic Nanomaterials for Diagnostic, Therapeutic, and Theranostic Applications," *Adv. Mater.* **30**(10), 1701460 (2018).
20. P. Singh, S. Pandit, V. R. S. S. Mokkapati, A. Garg, V. Ravikumar, and I. Mijakovic, "Gold Nanoparticles in Diagnostics and Therapeutics for Human Cancer," *Int. J. Mol. Sci.* **19**(7), 1797 (2018).
21. F. SM, and H. Banu, "Gold Nanoparticles in Cancer Diagnosis and Treatment: A Review," *Austin Journal of Biotechnology & Bioengineering* **1** (2015).
22. M. Khorasaninejad and F. Capasso, "Metalenses: Versatile multifunctional photonic components," *Science* **358**(6367), eaam8100 (2017).
23. X. Luo, "Subwavelength Optical Engineering with Metasurface Waves," *Adv. Opt. Mater.* **6**(7), 1701201 (2018).
24. M. L. Tseng, H.-H. Hsiao, C. H. Chu, M. K. Chen, G. Sun, A.-Q. Liu, and D. P. Tsai, "Metalenses: Advances and Applications," *Adv. Opt. Mater.* **6**(18), 1800554 (2018).
25. K. Aydin, V. E. Ferry, R. M. Briggs, and H. A. Atwater, "Broadband polarization-independent resonant light absorption using ultrathin plasmonic super absorbers," *Nat. Commun.* **2**(1), 517 (2011).
26. Y. X. Cui, J. Xu, K. H. Fung, Y. Jin, A. Kumar, S. L. He, and N. X. Fang, "A thin film broadband absorber based on multi-sized nanoantennas," *Appl. Phys. Lett.* **99**(25), 253101 (2011).
27. S. Kang, Z. Qian, V. Rajaram, A. Alu, and M. Rinaldi, "Ultra narrowband infrared absorbers for omnidirectional and polarization insensitive multi-spectral sensing microsystems," in 2017 19th International Conference on Solid-State Sensors, Actuators and Microsystems (TRANSDUCERS)(2017), pp. 886–889.
28. B. M. Adomanis, C. M. Watts, M. Koirala, X. Liu, T. Tyler, K. G. West, T. Starr, J. N. Bringuier, A. F. Starr, N. M. Jokerst, and W. J. Padilla, "Bi-layer metamaterials as fully functional near-perfect infrared absorbers," *Appl. Phys. Lett.* **107**(2), 021107 (2015).
29. F. Yi, E. Shim, A. Y. Zhu, H. Zhu, J. C. Reed, and E. Cubukcu, "Voltage tuning of plasmonic absorbers by indium tin oxide," *Appl. Phys. Lett.* **102**(22), 221102 (2013).
30. J. Goh, I. Fushman, D. Englund, and J. Vučković, "Genetic optimization of photonic bandgap structures," *Opt. Express* **15**(13), 8218–8230 (2007).
31. S. Preble, M. Lipson, and H. Lipson, "Two-dimensional photonic crystals designed by evolutionary algorithms," *Appl. Phys. Lett.* **86**(6), 061111 (2005).
32. J. Lu and J. Vučković, "Nanophotonic computational design," *Opt. Express* **21**(11), 13351–13367 (2013).
33. A. Y. Piggott, J. Lu, K. G. Lagoudakis, J. Petykiewicz, T. M. Babinec, and J. Vučković, "Inverse design and demonstration of a compact and broadband on-chip wavelength demultiplexer," *Nat. Photonics* **9**(6), 374–377 (2015).
34. L. Su, R. Trivedi, N. V. Sapra, A. Y. Piggott, D. Vercruyse, and J. Vučković, "Fully-automated optimization of grating couplers," *Opt. Express* **26**(4), 4023–4034 (2018).
35. Z. Lin, X. Liang, M. Lončar, S. G. Johnson, and A. W. Rodriguez, "Cavity-enhanced second-harmonic generation via nonlinear-overlap optimization," *Optica* **3**(3), 233–238 (2016).

36. Z. Lin, M. Lončar, and A. W. Rodriguez, "Topology optimization of multi-track ring resonators and 2D microcavities for nonlinear frequency conversion," *Opt. Lett.* **42**(14), 2818–2821 (2017).
37. D. Sell, J. Yang, S. Doshay, R. Yang, and J. A. Fan, "Large-Angle, Multifunctional Metagratings Based on Freeform Multimode Geometries," *Nano Lett.* **17**(6), 3752–3757 (2017).
38. B. Shen, P. Wang, R. Polson, and R. Menon, "Ultra-high-efficiency metamaterial polarizer," *Optica* **1**(5), 356–360 (2014).
39. J. Kennedy and R. Eberhart, "Particle swarm optimization," in *Neural Networks, 1995. Proceedings., IEEE International Conference on*(1995), pp. 1942–1948 vol.1944.
40. J. Robinson and Y. Rahmat-Samii, "Particle Swarm Optimization in Electromagnetics," *IEEE Trans. Antenn. Propag.* **52**(2), 397–407 (2004).
41. V. Gruev, R. Perkins, and T. York, "CCD polarization imaging sensor with aluminum nanowire optical filters," *Opt. Express* **18**(18), 19087–19094 (2010).
42. M. Kulkarni and V. Gruev, "Integrated spectral-polarization imaging sensor with aluminum nanowire polarization filters," *Opt. Express* **20**(21), 22997–23012 (2012).
43. Y. Zhao, C. Yi, S. G. Kong, Q. Pan, and Y. Cheng, "Multi-band polarization imaging and applications," *J. Sens.* **2016**, 1 (2016).
44. J. S. Tyo, D. L. Goldstein, D. B. Chenault, and J. A. Shaw, "Review of passive imaging polarimetry for remote sensing applications," *Appl. Opt.* **45**(22), 5453–5469 (2006).
45. S. A. Kemme, A. A. Cruz-Cabrera, R. R. Boye, T. Carter, S. Samora, C. Alford, J. R. Wendt, G. A. Vawter, and J. L. Smith, "Micropolarizing device for long wavelength infrared polarization imaging," presented at the Sandia Report SAND2006-6889, Sandia National Lab. Albuquerque, NM2006.
46. G. P. Nordin, J. T. Meier, P. C. Deguzman, and M. W. Jones, "Micropolarizer array for infrared imaging polarimetry," *J. Opt. Soc. Am. A* **16**(5), 1168–1174 (1999).
47. E. Arbabi, S. M. Kamali, A. Arbabi, and A. Faraon, "Full-Stokes Imaging Polarimetry Using Dielectric Metasurfaces," *ACS Photonics* **5**(8), 3132–3140 (2018).
48. G. P. Nordin, J. T. Meier, P. C. Deguzman, and M. W. Jones, "Micropolarizer array for infrared imaging polarimetry," *J. Opt. Soc. Am. A* **16**(5), 1168–1174 (1999).
49. A. G. Andreou and Z. K. Kalayjian, "Polarization imaging: principles and integrated polarimeters," *IEEE Sens. J.* **2**(6), 566–576 (2002).
50. T. York and V. Gruev, "Optical characterization of a polarization imager," in *International Symposium on Circuits and Systems*(2011), pp. 1576–1579.
51. B. J. Lee, L. P. Wang, and Z. M. Zhang, "Coherent thermal emission by excitation of magnetic polaritons between periodic strips and a metallic film," *Opt. Express* **16**(15), 11328–11336 (2008).
52. C. Wu, I. Burton Neuner, G. Shvets, J. John, A. Milder, B. Zollars, and S. Savoy, "Large-area wide-angle spectrally selective plasmonic absorber," *Phys. Rev. B Condens. Matter Mater. Phys.* **84**(7), 075102 (2011).
53. G. Baffou, C. Girard, and R. Quillard, "Mapping heat origin in plasmonic structures," *Phys. Rev. Lett.* **104**(13), 136805 (2010).
54. G. Baffou and R. Quillard, "Thermo-plasmonics: using metallic nanostructures as nano-sources of heat," *Laser Photonics Rev.* **7**(2), 171–187 (2013).
55. Y. K. Zhong, S. M. Fu, W. Huang, D. Rung, J. Y.-W. Huang, P. Parashar, and A. Lin, "Polarization-selective ultra-broadband super absorber," *Opt. Express* **25**(4), A124–A133 (2017).
56. C. Wu and G. Shvets, "Design of metamaterial surfaces with broadband absorbance," *Opt. Lett.* **37**(3), 308–310 (2012).
57. S. Wang, Y. Wang, S. Zhang, and W. Zheng, "Mid-infrared broadband absorber of full semiconductor epi-layers," *Phys. Lett. A* **381**(16), 1439–1444 (2017).
58. N. Jin and Y. Rahmat-Samii, "Particle Swarm Optimization for Antenna Designs in Engineering Electromagnetics," *J. Artif. Evol. Appl.* **2008**, 1 (2008).
59. E. D. Palik, *Handbook of Optical Constants of Solids* (Academic, 1985).
60. J. A. Schuller, E. S. Barnard, W. Cai, Y. C. Jun, J. S. White, and M. L. Brongersma, "Plasmonics for extreme light concentration and manipulation," *Nat. Mater.* **9**(3), 193–204 (2010).